ChemComm

COMMUNICATION

View Article Online
View Journal | View Issue

Cite this: *Chem. Commun.*, 2023, **59**, 4660

Received 27th February 2023,
Accepted 22nd March 2023

DOI: 10.1039/d3cc00953j

rsc.li/chemcomm

How fast do defects migrate in halide perovskites: insights from on-the-fly machine-learned force fields†

Mike Pols, Victor Brouwers, Sofía Calero and Shuxia Tao *

The migration of defects plays an important role in the stability of halide perovskites. It is challenging to study defect migration with experiments or conventional computer simulations. The former lacks an atomic-scale resolution and the latter suffers from short simulation times or a lack of accuracy. Here, we demonstrate that machine-learned force fields, trained with an on-the-fly active learning scheme against accurate density functional theory calculations, allow us to probe the differences in the dynamical behaviour of halide interstitials and halide vacancies in two closely related compositions $CsPbI_3$ and $CsPbBr_3$. We find that interstitials migrate faster than vacancies, due to the shorter migration paths of interstitials. Both types of defects migrate faster in $CsPbI_3$ than in $CsPbBr_3$. We attribute this to the less compact packing of the ions in $CsPbI_3$, which results in a larger motion of the ions and thus more frequent defect migration jumps.

Despite the rapid developments of halide perovskite optoelectronic devices,[1,2] the poor stability of the material remains a major obstacle for large scale applications. These stability problems include material decomposition,[3] halide segregation[4] and ion accumulation at interfaces,[5] all of which involve the migration of point defects. In experiments, the motion of ions and defects can be probed directly through impedance spectroscopy[6] or indirectly through changes in optoelectronic properties, *i.e.* the band gap.[7] Although experiments provide valuable information on the macroscopic behaviour, the identification of their microscopic properties is challenging. Various computational studies have provided microscopic insights into the defects, such as the type and concentration of defects in halide perovskites,[8] defect migration[9] and defect-induced degradation at perovskite grain boundaries.[10] However, the too high computational cost of *ab initio* methods and the limited accuracy of empirical force fields has prevented conventional computational methods from studying the subtle effects of the defect type and changes in composition on the defect migration rates, which remain an unclear and debated subject.[11–15]

Machine-learned force fields (MLFFs) have emerged as an attractive computational method to investigate the dynamics of complex materials at an accuracy that is close to *ab initio* methods.[16,17] MLFFs typically require an extensive amount of reference data in the training set, making their construction non-trivial and laborious. As a result of this, on-the-fly learning schemes, that generate training sets with minimal human intervention have become popular.[18–20] During an on-the-fly training, high-error atomic configurations, identified by Bayesian uncertainty predictions, are continuously added to the training set during a molecular dynamics (MD) run with the current best model. This scheme has proven to be robust and accurate for studying the lattice dynamics of halide perovskites, including phase transitions and cation rotations,[21,22] but their application to complex defect processes in perovskites has not yet been explored.

In this work, we employ on-the-fly trained MLFFs to investigate defect migration in halide perovskites. From extensive testing, we conclude that the transferability of MLFFs can not be assumed, and a high accuracy can only be achieved if it is explicitly trained against the exact defect type and chemical composition of interest. Using $CsPbX_3$ (X = I/Br) as model systems, we demonstrate that MLFFs can probe the effects of the defect type (interstitial or vacancy) and perovskite composition ($CsPbI_3$ or $CsPbBr_3$) on the dynamical behaviour of these defects. From an analysis of the MD simulations, we connect the differences in the diffusion rates to the typical motion of the ions in the lattice.

We use the FLARE++ package[19,20] to train sparse Gaussian process (SGP) models using the multielement atomic cluster expansion[23] to map the local atomic environments. Whenever the Bayesian error estimate of the model exceeds a threshold, a density functional theory (DFT) calculation at the generalized gradient approximation (GGA) level is performed in VASP[24–26]

Materials Simulation & Modelling, Department of Applied Physics, Eindhoven University of Technology, Eindhoven 5600 MB, The Netherlands.
E-mail: s.x.tao@tue.nl

† Electronic supplementary information (ESI) available: Computational methods, on-the-fly training procedures, model validations and production simulations. See DOI: https://doi.org/10.1039/d3cc00953j

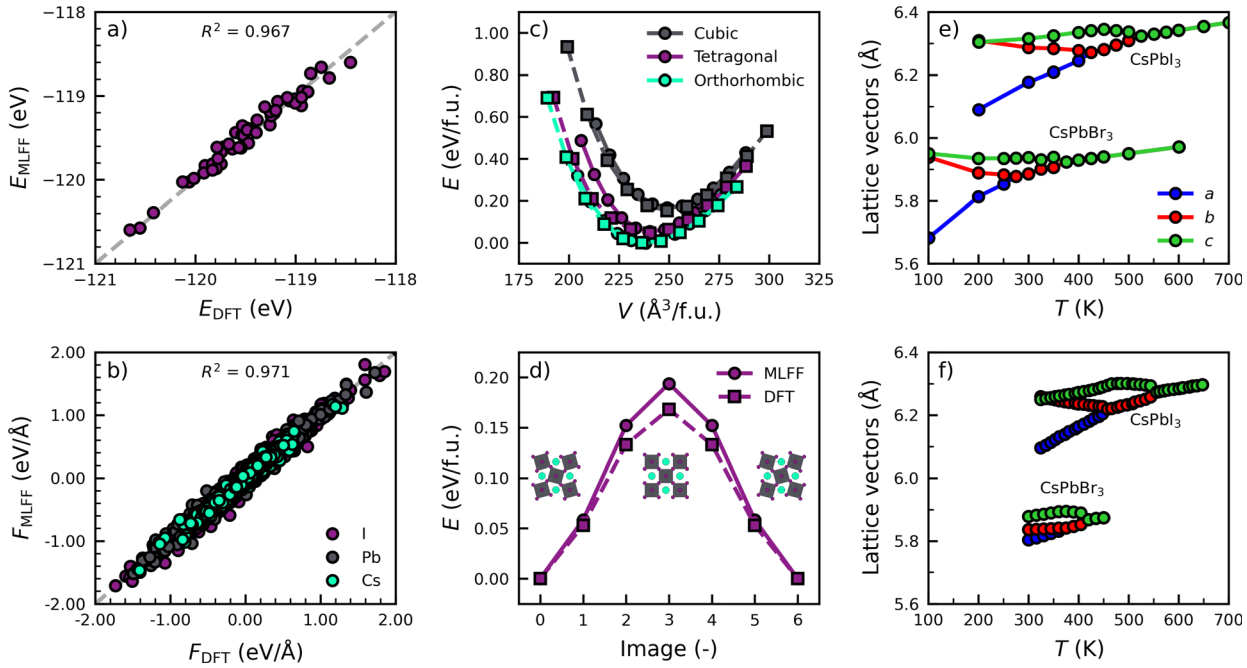

Fig. 1 Comparison of the performance of the MLFF trained against three phases of $CsPbI_3$ with DFT calculations. Parity plots of (a) energies and (b) atom-decomposed forces from snapshots of a high-temperature (700 K) simulation of $CsPbI_3$ at atmospheric pressure. (c) Equations of state of three black phases of $CsPbI_3$ from DFT (squares) and MLFF (circles). (d) Octahedral inversion barrier in tetragonal $CsPbI_3$. Phase diagrams for $CsPbI_3$ and $CsPbBr_3$ from (e) MLFF simulations and (f) experiments.

and its energies, forces and stresses are added to the training set and the model is retrained. To increase the efficiency with which the models can be evaluated, the MLFF predictions are mapped onto low-dimensional polynomial models after training according to the procedure outlined by Xie *et al.*[27] The accuracy of the resulting models is then assessed by comparing their atomic force and total energy predictions with those from DFT calculations. Subsequently, the mapped models are used in large-scale MD simulations with LAMMPS.[28] A description of the theory of SGP models and computational settings of the DFT calculations and large-scale MD simulations can be found in Note 1 (ESI†).

We start by training two models for both perovskite compositions, *i.e.* $CsPbI_3$ and $CsPbBr_3$, to describe the characteristic phase transitions between the various photoactive phases (cubic, tetragonal and orthorhombic).[29,30] To efficiently sample configurations in each phase, we train from a high to low temperatures, resulting in the inclusion of 163, 62, 472 local environments in the training set for Cs, Pb and I, respectively. The full details of the model training and validation can be found in Note 2 (ESI†). To check the accuracy of the models, we compare the energies and force components of the $CsPbI_3$ model with those from DFT calculations in Fig. 1a and b. We evaluate 50 equally spaced frames from a simulation of at 700 K and atmospheric pressure. The high values of the coefficient of determination, $R^2 = 0.967$ and $R^2 = 0.971$, for the parity of the energies and forces, respectively, illustrate the high accuracy of the models. This is further confirmed by the low mean absolute errors (MAEs) in the energies (1.8 meV per atom) and forces (0.044 eV Å^{-1}), comparable to those for various materials in literature.[18,20,21]

In addition, our models accurately replicate two important properties relevant to its phase behaviour in Fig. 1c and d. Specifically, the model accurately predicts the relative energies of the different perovskite phases, the orthorhombic phase as the most stable, followed by the tetragonal and cubic phase. Furthermore, a good agreement is found between the model and DFT calculations in tetragonal $CsPbI_3$ for the bulk modulus ($B_{0,MLFF}$ = 18.3 GPa; $B_{0,DFT}$ = 14.2 GPa) and the inversion barrier of PbI_6 octahedra (ΔE_{MLFF} = 0.19 eV; ΔE_{DFT} = 0.17 eV), of which more details are found in Note 2 (ESI†). Finally, we use the models to simulate the phase transitions of $CsPbI_3$ and $CsPbBr_3$. In Fig. 1e and f, we monitor the evolution of the lattice parameters as a function of the temperature and compare them with experiments.[29,30] The details of the simulations are found in Note 3 (ESI†). The comparison shows an excellent qualitative agreement. Not only do the models correctly predict the order in which the phases occur, they also correctly describe that $CsPbBr_3$ has phase transitions at lower temperatures than $CsPbI_3$.[29,30] We note that the models slightly underpredict the experimental phase transition temperatures (<100 K), which we attribute to a slight overprediction of the lattice volume by our models of about 3% for $CsPbI_3$ and 4% for $CsPbBr_3$ compared to experiments.

Next we assess the transferability of the models trained for the phase transitions in pristine perovskites to defective lattices, *i.e.* $CsPbI_3$ with an iodide vacancy as shown in Fig. 2a. To do so, we compare the forces predicted by the MLFF against results obtained from DFT calculations in Fig. 2b. Subsequently, we make a similar comparison for a model explicitly trained against $CsPbI_3$ with an iodide vacancy in Fig. 2c. The full details

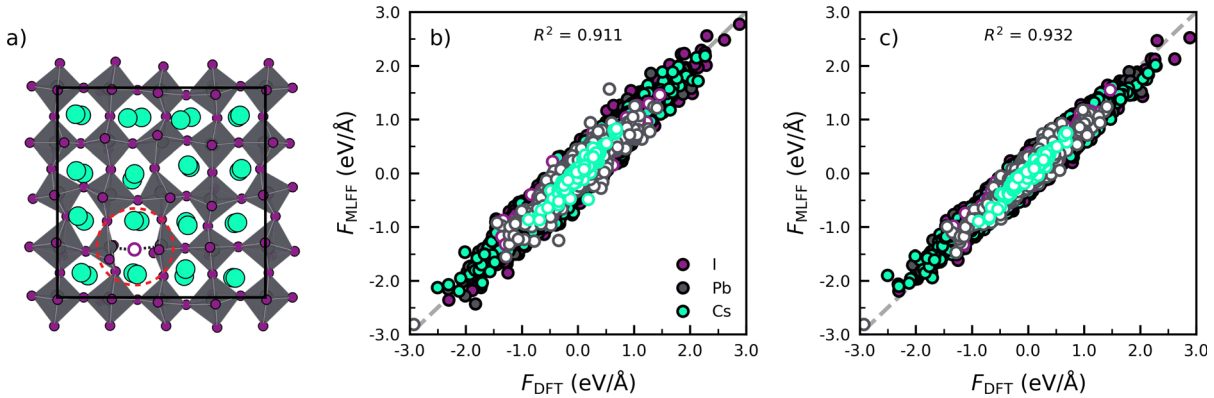

Fig. 2 (a) Structure of bulk $CsPbI_3$ with an iodide vacancy (V_I). The iodide vacancy is indicated by the purple circle and the local defect region by the red dashed circle. Parity plots of the atom-decomposed force components from the (b) phase transition-trained model and (c) vacancy-trained model against DFT calculations on snapshots of a simulation at 750 K. Force components are indicated with coloured circles, for atoms close to the V_I defect (4.5 Å) in white circles with coloured edges.

of the simulations and analysis, defect model training and defect environment recognition can be found in Note 4 (ESI†).

Focusing on the model trained against the phase transitions of bulk $CsPbI_3$ first (Fig. 2b), we find that the MLFF captures the overall dynamical behaviour of the bulk perovskites, as evidenced by the high value of R^2 = 0.911 for the force predictions. However, by distinguishing the force components for atoms close to and far away from the defect (r_{cut}^{def} = 4.5 Å; Note 4 in ESI†), we find a considerable decrease in R^2 when going from a bulk environment ($R_{bulk}{}^2$ = 0.914) to the defect environment ($R_{defect}{}^2$ = 0.843). This indicates that the phase transition model lacks accuracy for the description of environment near the defects. A further analysis of the R^2 individual atomic species, shows that near the vacancy defect, Pb ($R_{Pb}{}^2$ = 0.822) and I ($R_I{}^2$ = 0.857) force components are poorly described due to the breaking of a Pb–I bond. Noticeably, an explicit training of the MLFF on $CsPbI_3$ with a halide vacancy can decrease the errors and lead to improved R^2 values for Pb ($R_{Pb}{}^2$ = 0.888) and I ($R_I{}^2$ = 0.915) and an overall higher value of R^2 = 0.932 for the full system. Altogether, the analysis confirms that the retraining incorporates atomic configurations that represent the defects, thus improving the accuracy of the description of the defects.

Following the above analysis, we now train four new MLFFs, each tailored to studying a specific type of halide defects (vacancies and interstitials) in $CsPbI_3$ and $CsPbBr_3$. With these models, the defect dynamics in model systems with two point defects per 256 formula units are investigated, resulting in a defect concentration of 3–4 $\times$ 10^{19} cm^{-3}. We focus on the migration of defects at relatively high temperatures ranging from 550 K to 750 K. This is to ensure that defect migration can occur during our 2.5 ns simulations and to exclude the effects of phase transitions. The training procedure and production simulations are detailed in Note 5 (ESI†). The temperature dependence of the diffusion coefficients is shown in Fig. 3a. We analyze the temperature evolution of the diffusion coefficients D with an Arrhenius relation.[31]

$$D = D_0 \cdot \exp\left(-\frac{E_a}{k_B T}\right) \quad (1)$$

with D_0 as the diffusion prefactor, E_a the activation energy and k_B the Boltzmann constant. An overview of the obtained analysis parameters is found in Table 1.

We observe that interstitials generally migrate faster than vacancies. This follows from a combined higher diffusion attempt frequency (D_0) and lower diffusion migration barrier (E_a). We explain this observation using the differences in the migration pathways of the two types of defects, schematic overviews of which are found in Fig. 3b and c for $CsPbI_3$. Although both defects require the rotation of a halide ion around a Pb ion, the migration pathway for interstitials (2.2 Å) is substantially shorter than that for vacancies (4.5 Å). This difference stems from the fact that vacancies occupy a single lattice site (Fig. 3b), whereas the interstitial geometry is an iodide bridge geometry (Fig. 3c) in which two iodide ions occupy a single lattice site that results in an approximate halving of the distance to be covered by the point defect upon migration. As a result of their slower migration, the self-diffusion coefficients of halide vacancies in Fig. 3a exhibit a larger spread than those of the halide interstitials.

Moreover, we find that defects are more prone to migration in $CsPbI_3$ than in $CsPbBr_3$. We explain this observation by the more compact crystal packing in $CsPbBr_3$ than in $CsPbI_3$, also reflected by the higher Goldschmidt tolerance factor for $CsPbBr_3$ (0.82) when compared to $CsPbI_3$ (0.81).[32] The more compact crystal packing results in a smaller amount of freedom for the ions to move (Fig. 3d). As such, the halide ions exhibit an overall lower mobility in the perovskite lattice, which is further supported by analyses of the scaled root mean squared displacement (RMSD) of the halide ions (Note 3 in ESI†) confirming that Br ions in $CsPbBr_3$ show considerably less motion (0.165) than I ions in $CsPbI_3$ (0.185). We note that the degree of motion of the halide ions depends closely on the phase of the perovskite, in line with experimental reports,[33] where the diffusion dynamics of defects can vary between the different phases.

In summary, we demonstrate that on-the-fly trained MLFFs can accurately model defect migration in inorganic halide perovskites. The high accuracy and efficiency of these models

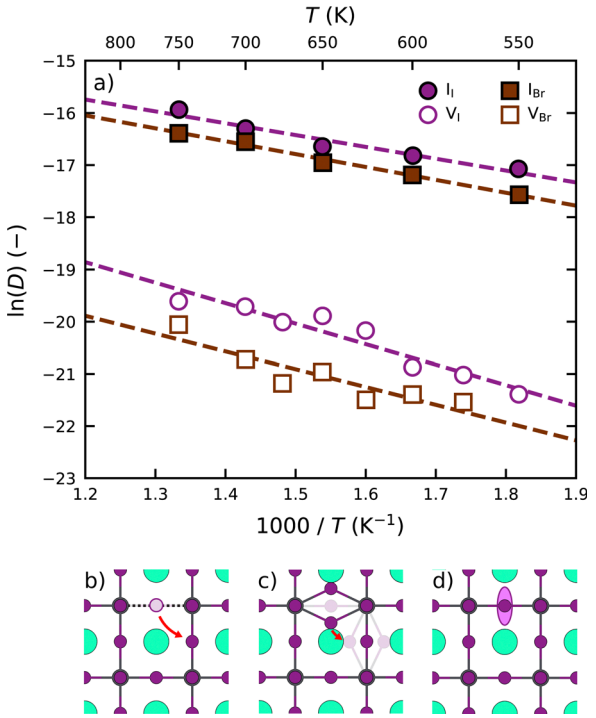

Fig. 3 (a) Temperature evolution of self-diffusion coefficients of halide vacancies (V_X; white symbols) and halide interstitials (I_X; coloured symbols) in $CsPbX_3$. The defect migration pathways of (b) V_I and (c) I_I defects in $CsPbI_3$, with both the initial and final structures. (d) The typical motion of halide species in the perovskite lattice.

Table 1 Overview of the diffusion parameters D_0 and E_a for halide vacancies (V_X) and halide interstitials (I_X) in $CsPbI_3$ and $CsPbBr_3$

Perovskite	Defect	D_0 ($\times 10^{-6}$ s)	E_a (eV)
$CsPbI_3$	V_I	0.7 ± 0.5	0.34 ± 0.04
$CsPbI_3$	I_I	2.2 ± 1.0	0.20 ± 0.02
$CsPbBr_3$	V_{Br}	0.1 ± 0.2	0.29 ± 0.06
$CsPbBr_3$	I_{Br}	2.0 ± 0.5	0.21 ± 0.01

allow us to identify the qualitative trends in migration rates of different defect types in different chemical compositions. We find that interstitials are more mobile than vacancies and that both types of defects migrate faster in $CsPbI_3$ than in $CsPbBr_3$. Moreover, we highlight that the transferability of the models can not be assumed and a high accuracy can only be achieved once explicitly trained against processes in the chemical environment of interest.

We acknowledge SURF for providing computational resources (Project No. EINF-2160). S. T. acknowledges funding from START-UP (Project No. 740.018.024) and Vidi (Project No. VI.Vidi.213.091) from the Dutch Research Council (NWO).

Conflicts of interest

There are no conflicts to declare.

References

1 M. Kim, J. Jeong, H. Lu, T. K. Lee, F. T. Eickemeyer, Y. Liu, I. W. Choi, S. J. Choi, Y. Jo, H.-B. Kim, S.-I. Mo, Y.-K. Kim, H. Lee, N. G. An, S. Cho, W. R. Tress, S. M. Zakeeruddin, A. Hagfeldt, J. Y. Kim, M. Grätzel and D. S. Kim, *Science*, 2022, **375**, 302–306.
2 A. Fakharuddin, M. K. Gangishetty, M. Abdi-Jalebi, S.-H. Chin, A. R. bin Mohd Yusoff, D. N. Congreve, W. Tress, F. Deschler, M. Vasilopoulou and H. J. Bolink, *Nat. Electron.*, 2022, **5**, 203–216.
3 Z. Ni, H. Jiao, C. Fei, H. Gu, S. Xu, Z. Yu, G. Yang, Y. Deng, Q. Jiang, Y. Liu, Y. Yan and J. Huang, *Nat. Energy*, 2022, **7**, 65–73.
4 A. J. Knight and L. M. Herz, *Energy Environ. Sci.*, 2020, **13**, 2024–2046.
5 J. Li, Q. Dong, N. Li and L. Wang, *Adv. Energy Mater.*, 2017, **7**, 1602922.
6 A. Guerrero, J. Bisquert and G. Garcia-Belmonte, *Chem. Rev.*, 2021, **121**, 14430–14484.
7 K. Datta, B. T. van Gorkom, Z. Chen, M. J. Dyson, T. P. A. van der Pol, S. C. J. Meskers, S. Tao, P. A. Bobbert, M. M. Wienk and R. A. J. Janssen, *ACS Appl. Energy Mater.*, 2021, **4**, 6650–6658.
8 H. Xue, G. Brocks and S. Tao, *Phys. Rev. Mater.*, 2022, **6**, 055402.
9 N. Phung, A. Al-Ashouri, S. Meloni, A. Mattoni, S. Albrecht, E. L. Unger, A. Merdasa and A. Abate, *Adv. Energy Mater.*, 2020, **10**, 1903735.
10 M. Pols, T. Hilpert, I. A. Filot, A. C. T. van Duin, S. Calero and S. Tao, *ACS Appl. Mater. Interfaces*, 2022, **14**, 40841–40850.
11 C. Lin, S. Li, W. Zhang, C. Shao and Z. Yang, *ACS Appl. Energy Mater.*, 2018, **1**, 1374–1380.
12 S. R. G. Balestra, J. M. Vicent-Luna, S. Calero, S. Tao and J. A. Anta, *J. Mater. Chem. A*, 2020, **8**, 11824–11836.
13 J. M. Azpiroz, E. Mosconi, J. Bisquert and F. D. Angelis, *Energy Environ. Sci.*, 2015, **8**, 2118–2127.
14 M. Pols, J. M. Vicent-Luna, I. Filot, A. C. T. van Duin and S. Tao, *J. Phys. Chem. Lett.*, 2021, **12**, 5519–5525.
15 P. Delugas, C. Caddeo, A. Filippetti and A. Mattoni, *J. Phys. Chem. Lett.*, 2016, **7**, 2356–2361.
16 N. Artrith and A. M. Kolpak, *Comput. Mater. Sci.*, 2015, **110**, 20–28.
17 M. F. C. Andrade, H.-Y. Ko, L. Zhang, R. Car and A. Selloni, *Chem. Sci.*, 2020, **11**, 2335–2341.
18 R. Jinnouchi, F. Karsai and G. Kresse, *Phys. Rev. B*, 2019, **100**, 014105.
19 J. Vandermause, S. B. Torrisi, S. Batzner, Y. Xie, L. Sun, A. M. Kolpak and B. Kozinsky, *npj Comput. Mater.*, 2020, **6**, 1–11.
20 J. Vandermause, Y. Xie, J. S. Lim, C. J. Owen and B. Kozinsky, *Nat. Commun.*, 2022, **13**, 5183.
21 R. Jinnouchi, J. Lahnsteiner, F. Karsai, G. Kresse and M. Bokdam, *Phys. Rev. Lett.*, 2019, **122**, 225701.
22 H. Grüninger, M. Bokdam, N. Leupold, P. Tinnemans, R. Moos, G. A. De Wijs, F. Panzer and A. P. M. Kentgens, *J. Phys. Chem. C*, 2021, **125**, 1742–1753.
23 R. Drautz, *Phys. Rev. B*, 2019, **99**, 014104.
24 G. Kresse and J. Hafner, *Phys. Rev. B*, 1994, **49**, 14251–14269.
25 G. Kresse and J. Furthmüller, *Comput. Mater. Sci.*, 1996, **6**, 15–50.
26 G. Kresse and J. Furthmüller, *Phys. Rev. B*, 1996, **54**, 11169–11186.
27 Y. Xie, J. Vandermause, L. Sun, A. Cepellotti and B. Kozinsky, *npj Comput. Mater.*, 2021, **7**, 1–10.
28 A. P. Thompson, H. M. Aktulga, R. Berger, D. S. Bolintineanu, W. M. Brown, P. S. Crozier, P. J. in't Veld, A. Kohlmeyer, S. G. Moore, T. D. Nguyen, R. Shan, M. J. Stevens, J. Tranchida, C. Trott and S. J. Plimpton, *Comput. Phys. Commun.*, 2022, **271**, 108171.
29 C. C. Stoumpos, C. D. Malliakas, J. A. Peters, Z. Liu, M. Sebastian, J. Im, T. C. Chasapis, A. C. Wibowo, D. Y. Chung, A. J. Freeman, B. W. Wessels and M. G. Kanatzidis, *Cryst. Growth Des.*, 2013, **13**, 2722–2727.
30 A. Marronnier, G. Roma, S. Boyer-Richard, L. Pedesseau, J.-M. Jancu, Y. Bonnassieux, C. Katan, C. C. Stoumpos, M. G. Kanatzidis and J. Even, *ACS Nano*, 2018, **12**, 3477–3486.
31 S. Arrhenius, *Z. Phys. Chem.*, 1889, **4U**, 96–116.
32 S. Tao, I. Schmidt, G. Brocks, J. Jiang, I. Tranca, K. Meerholz and S. Olthof, *Nat. Commun.*, 2019, **10**, 1–10.
33 M. N. F. Hoque, N. Islam, Z. Li, G. Ren, K. Zhu and Z. Fan, *ChemSusChem*, 2016, **9**, 2692–2698.